RESEARCH ARTICLE

Microstructural evolution and oxidation in α/β titanium alloy under fretting fatigue loading

Hanqing LIU[1,2], **Xiaohong SHAO**[3], **Kai TAN**[1], **Zhenjie TENG**[4], **Yaohan DU**[1], **Lang LI**[1,*], **Qingyuan WANG**[1,*], **Qiang CHEN**[2]

[1] *Failure Mechanics and Engineering Disaster Prevention Key Laboratory of Sichuan Province, Sichuan University, Chengdu 610065, China*

[2] *Department of Mechanical Engineering, Kyushu University, Fukuoka 819-0395, Japan*

[3] *Shenyang National Laboratory for Materials Science, Institute of Metal Research, Chinese Academy of Sciences, Shenyang 110016, China*

[4] *Institute of Physical Chemistry, University of Münster, Münster 48149, Germany*

© The author(s) 2022.

Abstract: Coupling effects of fretting wear and cyclic stress could result in significant fatigue strength degradation, thus potentially causing unanticipated catastrophic fractures. The underlying mechanism of microstructural evolutions caused by fretting wear is ambiguous, which obstructs the understanding of fretting fatigue issues, and is unable to guarantee the reliability of structures for long-term operation. Here, fretting wear studies were performed to understand the microstructural evolution and oxidation behavior of an α/β titanium alloy up to 10^8 cycles. Contact surface degradation is mainly caused by surface oxidation and the generation of wear debris during fretting wear within the slip zone. The grain size in the topmost nanostructured layer could be refined to ~40 nm. The grain refinement process involves the initial grain rotation, the formation of low angle grain boundary (LAGB; 2°–5°), the *in-situ* increments of the misorientation angle, and the final subdivision, which have been unraveled to feature the evolution in dislocation morphologies from slip lines to tangles and arrays. The formation of hetero microstructures regarding the nonequilibrium high angle grain boundary (HAGB) and dislocation arrays gives rise to more oxygen diffusion pathways in the topmost nanostructured layer, thus resulting in the formation of cracking interface to separate the oxidation zone and the adjoining nanostructured domain driven by tribological fatigue stress. Eventually, it facilitates surface degradation and the formation of catastrophic fractures.

Keywords: fretting wear; oxygen pick-up; dynamic recrystallization; grain rotation; low angle grain boundary (LAGB); grain refinement

1 Introduction

Titanium alloys with bimodal microstructures are extensively used in aero engines and critical rotating structures for their attractive combination of specific strength and fatigue resistance [1, 2]. However, their susceptibility to tribological damage has been recognized to assist in the potential fretting crack nucleation from the contact sites, leading to a significant reduction in fatigue strength of structures [3], which limits the applicability of titanium alloys [4, 5]. Tribological damage could take the form of plastic deformation [6], phase transformation [7, 8], and oxidation [9, 10] in the materials. Among them, plastic deformation and oxidation received extensive attention for their significant effects in generating the fretting cracks [11–16], and attempts were made to understand the mechanisms of microstructural evolution concerning

---

* Corresponding authors: Lang LI, E-mail: lilang@scu.edu.cn; Qingyuan WANG, E-mail: wangqy@scu.edu.cn

the tribological behavior of materials substantially.

Tribological damage occurs in the superficial layer of bulk material by forming debris and surface degradations within the contact area [17, 18]. Accordingly, the microstructure beneath the damaged area undergoes the grain refinement process against the extreme shearing stress, which may further alter the fretting wear performance of bulk material [19, 20]. To date, the governing deformation mechanisms involving grain rotation [12], dynamic recrystallization [21], activated slipping deformation [22], and twinning deformation [23] have been introduced to understand the tribology behavior of the materials. The associated changes in the alloying elements regarding surface oxidation and severe tribo-deformation are of great significance [8, 24, 25].

Generally, elementary mechanisms governing microstructural evolutions in materials subjected to the fretting fatigue loading remain elusive. Swalla et al. [6] reported that the grain refinement occurred to the tribo-deformed layer (TDL) of Ti–6Al–4V, and the volume fraction of low angle grain boundary (LAGB) was measured to be orders of magnitude higher than that of the underneath bulk materials. Incipient tribo-deformation takes its shape in the form of grain rotation in association with the formation of subgrains [12]. Furtherly, recrystallized nanostructures could be well established with negligible residual plastic strain inside [24]. However, fretting fatigue cracks prefer to nucleate along the highly deformed band beneath the contact site [26], and the grains adjacent to the fretting fatigue crack extension path are severely strained and exhibit high grain reference orientation deviation (GROD) values [27]. The dynamic recrystallization process of grains in the TDL from initial coarse structures to well-established nanograins has not been fundamentally studied in the literature, leaving a gap in understanding the fretting damage of metallic materials.

Moreover, the oxygen enrichment in crack formation and early propagation domains indicates a significant role of tribo-oxidation in nucleating fretting fatigue cracks [27]. Nevertheless, the oxygen diffusion activity of materials that undergo tribo-deformation remains elusive. Strength degradation caused by impacts of contact stress associated with long-term cyclic stress necessitates a fundamental understanding of fretting damage and tribo-oxidation to ensure safety designs of load-bearing sectors [28]. On these bases, the present work aims to give a further understanding of the microstructural evolution and oxidation behavior of metallic material subjected to fretting fatigue loading.

2　Methods

2.1　Fretting wear test facility

Ultrasonic fatigue tester has been utilized to evaluate the tribological performance of metallic materials subjected to very high cycle fatigue loadings [29–32]. In this work, the fretting fatigue test of TC17 (Ti–5Al–2Sn–2Zr–4Mo–4Cr) titanium alloy was conducted with an ultrasonic torsional fatigue tester developed at Sichuan University [33]. Contact stress was applied on the specimen gauge section through fretting pads that were fabricated with the same material as the fatigue specimen, as indicated in Fig. 1. Cyclic loading was generated and transformed into the torsional mode, which was then amplified and imposed on the specimen that was designed to meet the resonance condition with the amplification horn [34]. During the test, the torsional displacement and shear stress distribution of the specimen surface are schematically illustrated in Fig. 1. The applied cyclic shear stress on the specimen surface was calibrated using a strain gauge before the fretting wear test, and the related procedures were detailed in Ref. [33].

2.2　Test material and fretting wear test procedures

The microstructures and alloy element distributions of the as-received TC17 alloy were analyzed by a scanning electron microscope (SEM; Ultra55, Zeiss) equipped with an energy dispersive spectrometer (X-max 150, Oxford Instruments) after mechanical polishing and etching to reveal the microstructures. The surface fully reversed cyclic shear stress τ_a of the specimen gauge section was set to an amplitude of 160 MPa during the fretting fatigue test, the associated cyclic displacement amplitude d_a between fretting pads and specimen surface was ~1.89 μm, and the applied normal load F_c through fretting pads was maintained at 22 N.
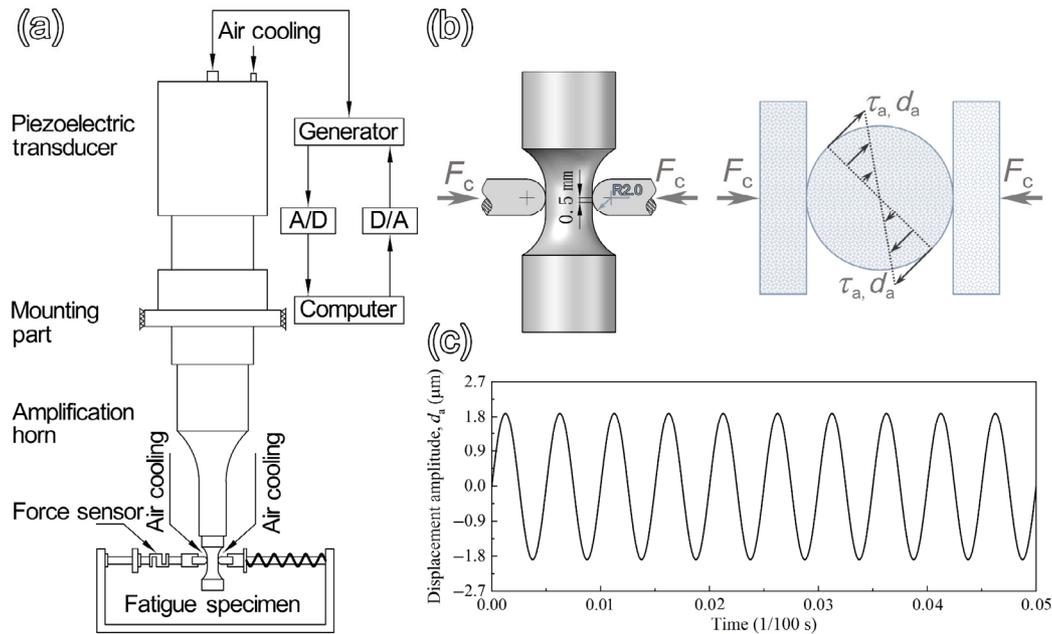
Fig. 1 (a) Schematic diagram of torsional fretting fatigue test system, (b) application of contact stress (F_c, τ_a, and d_a represent the applied normal load, surface fully reversed cyclic shear stress, and applied displacement amplitude, respectively), and (c) d_a during the fretting wear process.

2.3   Morphology of fretting wear damaged area

The morphologies of the worn areas with the accumulated loading cycles of 5×10^6, 1×10^7, 5×10^7, and 1×10^8 were measured with a white light interferometer (ContourGT-K, Bruker) and an SEM (JSM-6510LV, JEOL). The oxidation behavior of the damaged area was analyzed by the energy dispersive spectroscopy (EDS) in the SEM (Ultra55, Zeiss and X-max 150, Oxford Instruments) and the aberration-corrected scanning transmission electron microscope (STEM; JEM-ARM200F, JEOL).

2.4   Characterization of tribo-deformed microstructure

The tribo-deformed microstructure beneath the worn area was characterized using the transmission electron backscattered diffraction (t-EBSD) technic, and the data were collected using an EBSD detector (OIM-DVC5, EDAX) at an acceleration voltage of 30 kV, a step length of 10 nm, and a work distance of 5 mm. The lamella specimens were fabricated inside the slip and stick zones site-specifically using a focused ion beam (FIB; 3D 200i, Quanta) and thinned by an FIB (MI4000L, Hitachi). Further analysis of the deformation mechanism was performed on the lamella

specimens with a transmission electron microscope (TEM; JEM-2100HC, JEOL).

3   Results and discussion

3.1   Initial microstructure of TC17 alloy

The material studied in this work is a titanium alloy for turbine blade: TC17, of which the microstructure and associated alloy element distributions are shown in Fig. 2. The microstructure of the as-received TC17 alloy was tailored in a bimodal condition: equiaxed primary α (α_P) phase and secondary α lamellae (α_L) embedded in the prior β matrix. The grain size of α_P is ~3 μm, and the thickness of α_L is ~200 nm. α_P grains are enriched in the alloy element of Al, which performs as a kind of α stabilizer. On the contrary, the β stabilizers of Mo and Cr are segregated in the β grains. The alloy elements of Sn and Zr exhibit a general homogenous distribution in the material.

3.2   Wear scar observation

The evolution of fretting wear damaged area in the range of 5×10^6–1×10^8 cycles is demonstrated in Fig. 3. The evolution of torsional fretting damaged areas
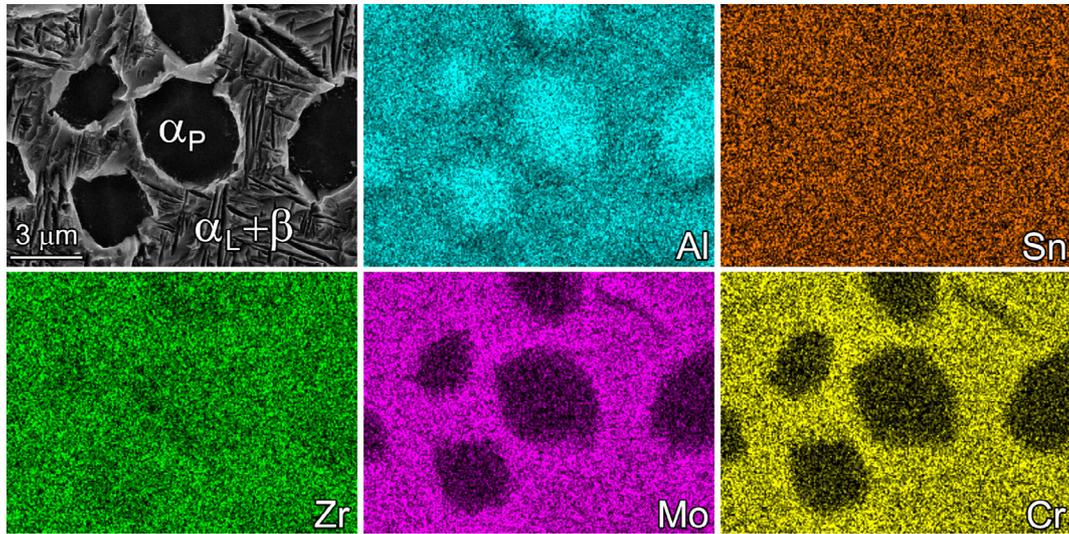
Fig. 2   SEM image of initial microstructure and alloy element distributions.
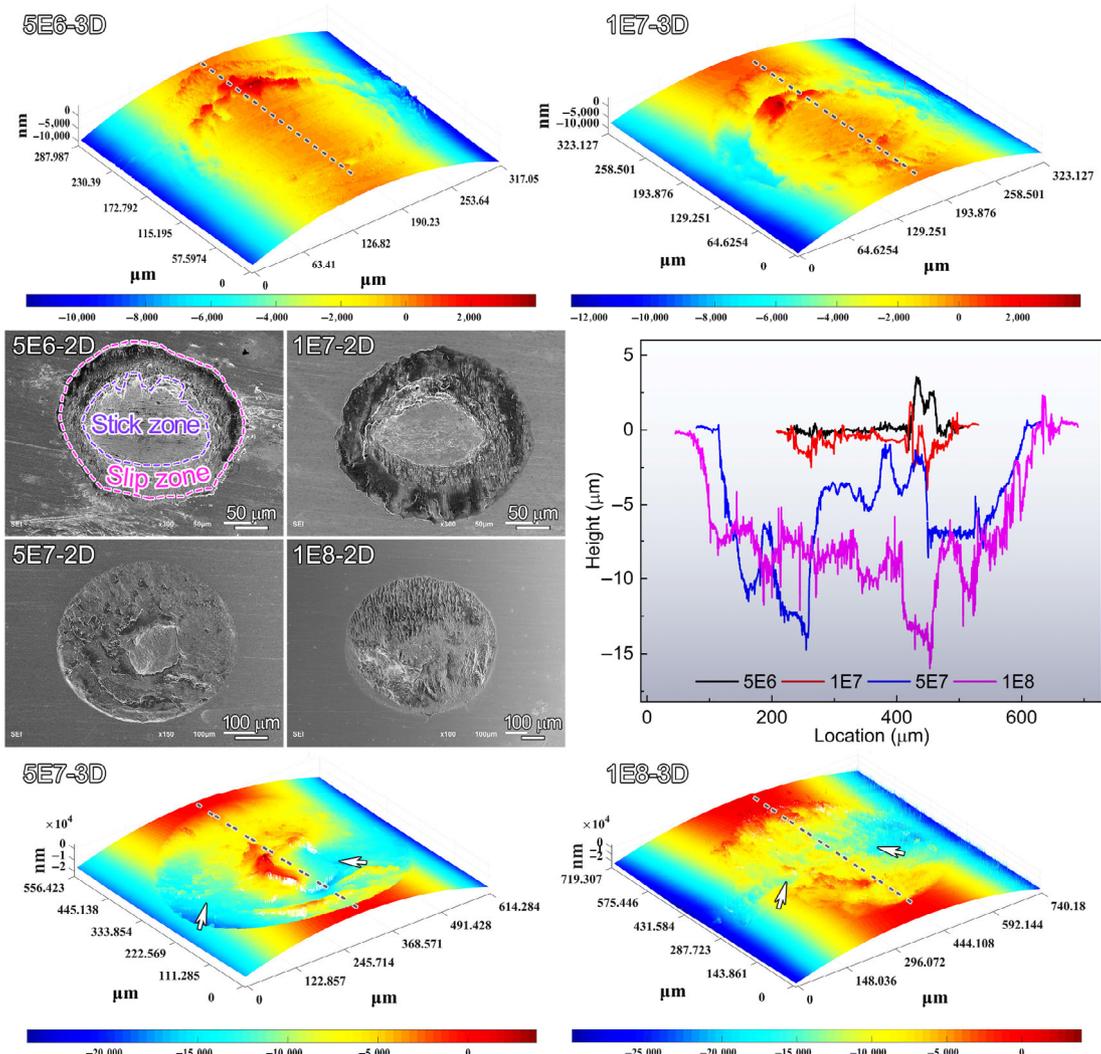

Fig. 3   Evolution of surface worn damaged area regarding morphology and depth as the wear cycle increases from 5×10^6 to 1×10^8 cycles under cyclic shear stress of 160 MPa.

with the accumulated fretting cycle regarding the morphology and dimension of the central stick zone and surrounded slip annular region was studied in the present work [35, 36], as displayed in the two-dimensional (2D) SEM results (Fig. 3). With the increase of the loading cycle at 160 MPa, the central stick zone diameter decreases from ~150 μm at 5×10^6 cycles to ~140 μm at 5×10^7 cycles gradually, and disappears with the loading cycle accumulating to 1×10^8 cycles. Accordingly, the accumulation of fretting fatigue loading expands the worn area outward of the slip zone centered on the contact site. The outer diameter of worn area develops from 245 μm at 5×10^6 cycles to ~520 μm at 5×10^7 cycles and ~635 μm at 1×10^8 cycles. Microcracks are generated along the contact area boundary after experiencing 5×10^7 and 1×10^8 cycles of fretting fatigue loading.

The three-dimensional (3D) topography of the fretting damaged area and the associated height profile along the indicated path are compared in Fig. 3. In general, the slip zone exhibits a higher roughness in comparison to the contact area because of more severe plastic deformation and the formation of wear debris in the annular deformed area [37]. As indicated by the arrows, wear pits appear on both sides of the stick zone at the loading cycles of 5×10^7 and 1×10^8. The evolution of fretting damage along the direction of F_c can be clarified by the wear depth evolution in the 2D profile curves (Fig. 3). In the early stage of the fretting damage process, a pronounced pile-up takes place at the upper edge of contact area. The fretting damage depth increases with the accumulation of fretting loading cycle, and is measured to be ~14.7 μm at 5×10^7 cycles and ~15.8 μm at 1×10^8 cycles.

During the fretting damage process, the size and depth of central contact area gradually decrease with the accumulation of fretting loading cycles. A conspicuous convex was generated after experiencing 5×10^7 cycles of fretting loading in the 2D profile curves (Fig. 3) due to the plastic flow accumulation [38], as well as the limitation of wear damage in the contact area. The evolution of worn area could furtherly alter contact stiffness [39]; for instance, the reduction of contact area could give rise to the shear stress at the contact interface [40], which promotes the further degradation of the contact size and wears

off the initial contact surface finally. Furthermore, the generated shear stress field at the contact interface exhibits an inhomogeneous distribution [41], of which the peak value at the boundary of the contact area could increase with the degradation of the contact area [40]. Localized overstressing during the fretting damage process leads to crack nucleation from the contact area boundary [42]. The surface degradation of the contact area at 5×10^7 and 1×10^8 loading cycles are estimated to be ~3 and 8 μm in depth, respectively, in comparison to those of the initial condition.

3.3 Tribo-oxidation behavior

Surface tribo-oxidation behavior was evaluated by the SEM–EDS over the fretting wear damaged area at 160 MPa for 5×10^7 cycles. An evident high concentration of oxygen is detected in the slip zone of the damaged area from the intensity distributions (Fig. 4(a)). The center of stick zone exhibits similar oxygen content information to the outer specimen surface due to the limited fretting wear displacement within the stick zone. The formation of oxide during the wearing process generates a hard protective layer within the slip zone [43], and the resistance against further wear damage in the slip zone is therefore promoted.

Further analysis of the oxidation behavior was performed on the localized area neighboring the interface of slip zone and contact zone that was enclosed by a dashed rectangle (Fig. 4(a)), of which the EDS mappings were presented in Fig. 4(b). Alloy element distributions (Fig. 4(b)) exhibit similar patterns distinguished by the matrix microstructure (Fig. 2), indicating the crystallographic integrity in the associated damaged area. By contrast, the heterogeneity in oxygen distribution suggests that the slip zone and stick zone experience different oxygen pick-up activities during the fretting wear process [44]. Oxygen-rich clusters were detected on both sides of the cracking interface of the contact and slip zone, indicating that the oxygen diffusion process occurred in the worn area before the abrasive deformation. The contact region that experiences tangential force may deform with plastic shearing [37], and associated traces can be recognized in Fig. 4(b). The localized dissipated thermal condition around the contact border may exceed the energy barrier for wear oxidation and
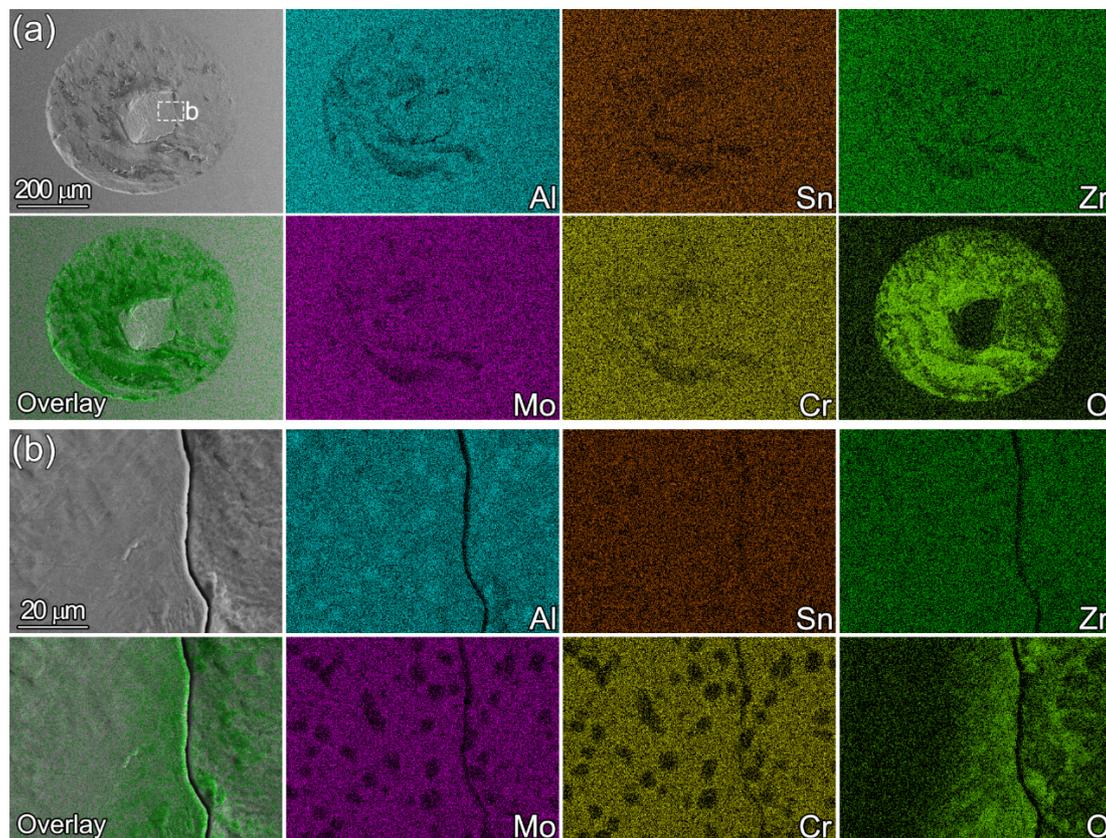
Fig. 4 Elemental distribution mappings over (a) damaged area and (b) cracking interface of contact and slip zones.

assist the deformed material in absorbing invasive oxygen.

Tribo-oxidized behavior in depth was studied by using the FIB and STEM–EDS, as presented in Fig. 5(a), and the site-specific TEM lamella was fabricated across the wear gully inside the slip zone of wear damaged area at 10^8 cycles. The microstructural delamination (Fig. 5(b)) can be categorized into three layers: the topmost layer with cavities, the TDL, and the general deformed layer (GDL). Figure 5(c) shows the STEM–EDS mappings covering the three layers. The porous layer beneath protective deposition layer presents a high concentration of oxygen element, therefore could be referred to as the oxidative layer (ODL). Besides, segments (indicated by the arrow) enriched with Ti and Al elements can be recognized within the oxidized layer, suggesting that the oxidized flake-off debris is the end product of the fretting wear process. Accordingly, the indicated flake-off segment exhibits a high concentration of Al element, which performs as an α stabilizer based on the aforementioned analysis (Fig. 2); as such, the segment

maintaining the lattice structure can be clarified to be the wear debris of α structure. The thickness of ODL in this area is ~1,200±200 nm.

The high angle annular dark-field (HAADF)-STEM image (Fig. 6) shows a crack in the bottom of the oxidization layer. A banded oxygen-enriched domain is revealed ahead of the crack tip by examining the localized EDS mappings in detail, suggesting that the incipient crack extends along the interface of the oxidative domain and bulk matrix. Besides, an aluminum-enriched particulate tends to be separated by the oxidative band from the adjacent matrix, indicating the coupling effects of oxidation and flake-off in the degradation of fretting wear surface. Heterogeneity in oxygen diffusion during the tribo-oxidation process has been documented to be sensitive to localized crystallographic features regarding the grains/phase boundaries, dislocations, and lattice orientation [25, 45, 46], thereby facilitating the formation of localized oxygen enrichment in the high diffusivity pathway. The increment of oxygen could decrease the ductility in titanium, and localized
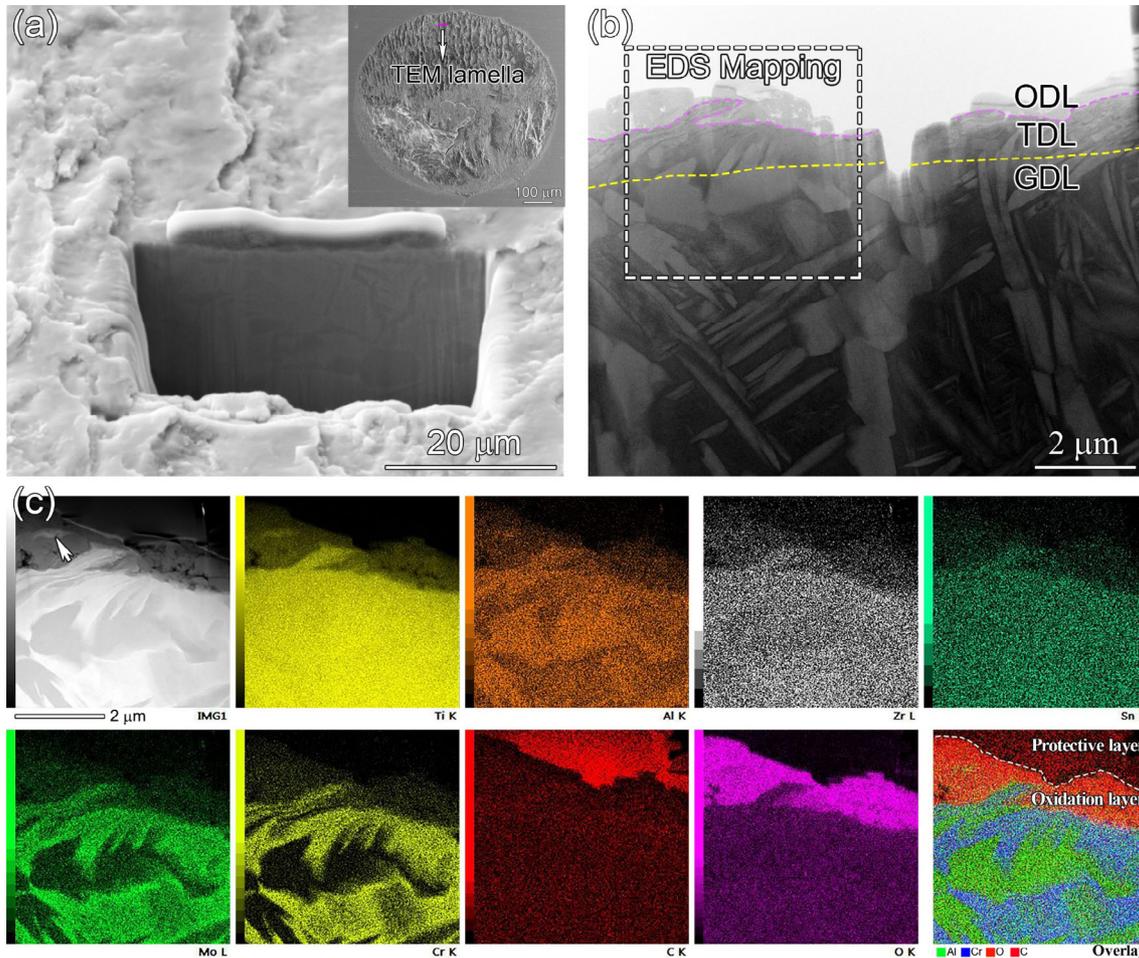
Fig. 5 (a) Position of the TEM sample, (b) annular bright field image of the thinned section in TEM lamella, and (c) STEM–EDS mappings showing the distributions of alloy elements, adsorbed oxygen, and protected carbon.

enrichment in oxygen could therefore alter the further strain response to the severe tribological shear stress by inhibiting the compatibility of plastic deformation [46, 47], leading to interfacial cracking [48]. Thereafter, the non-oxidized structures could be separated from the contact surface by crack extension, forming the flake-off particles within the ODL.

3.4 Tribo-deformation behavior

Tribo-deformed microstructures were analyzed to understand the microstructural evolution of α/β titanium alloy experiencing the fretting wear process. Figure 7(a) presents an SEM image of the sample fabricated in the central stick area that exhibits a lower roughness to the outer slip zone. The initial surface microstructures were removed from the counterface in the form of wear debris, and the

EBSD inverse pole figure (IPF) mapping (Fig. 7(b)) demonstrates the grain orientation of underlying microstructures of α_P and $\alpha_L+\beta$-colony beneath the contact surface. The microstructures in the outmost layer, especially within the α_P grain magnified with a finer scanning step (Fig. 7(c)), exhibit a gradient lattice orientation. The α_P structure, half of which has been worn off, is severely strained and exhibits delaminated strain accumulation revealed by the kernel averaged misorientation (KAM) mapping (Fig. 7(c)); but still, it maintains the initial coarse grain structure without generating nanostructured subgrains. Figure 7(d) gives the EBSD mappings of the $\alpha_L+\beta$-colony; the topmost layer is severely deformed, especially in the vicinity of α_L lamellar boundaries that exhibit a higher associated GROD value, indicating that the structure interfaces within the colony could shield strain
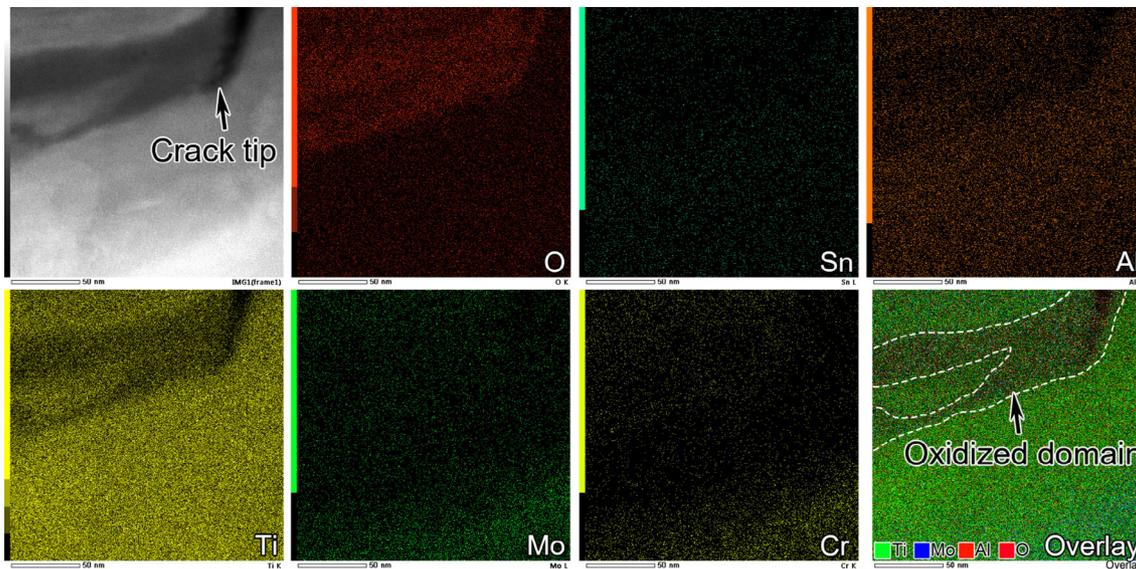
Fig. 6 HAADF-STEM image and STEM–EDS mappings showing the distributions of oxygen and alloy elements at the crack tip of the uppermost tribo-deformed layer.
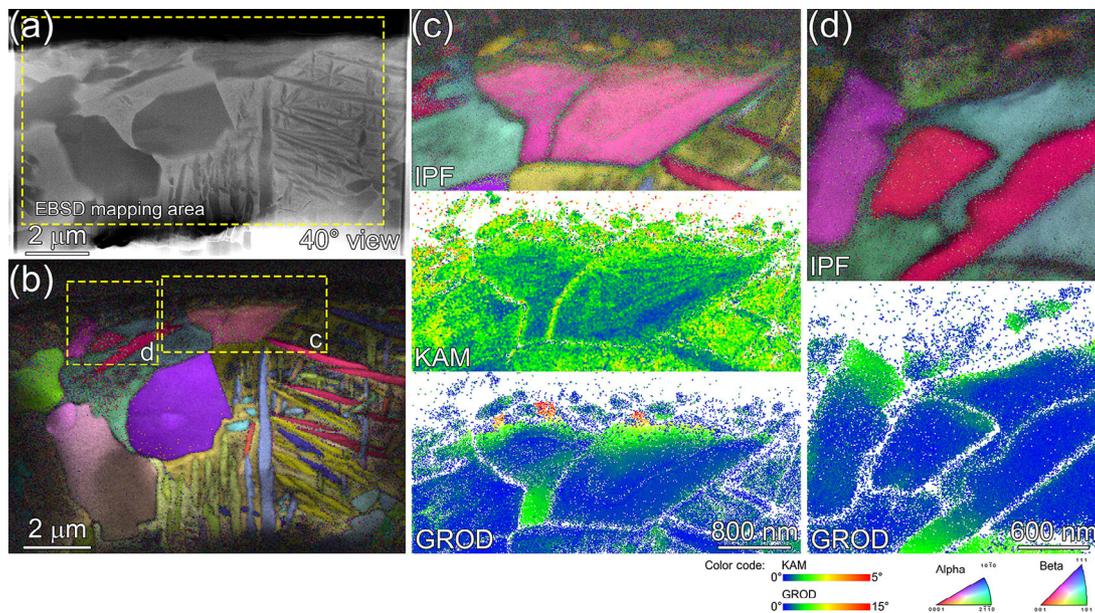

Fig. 7 (a) SEM image of site-specific TEM sample fabricating from the stick zone, (b) EBSD IPF mapping of the selected area in (a), (c) EBSD IPF, KAM, and GROD mappings of α_P grain in (b), and (d) EBSD IPF and GROD mappings of α_L+β-colony in (b).

against the tribo-deformation. While for the equiaxed α_P structure, as demonstrated by the EBSD GROD mapping (Fig. 7(c)), the accumulated inner strain presents in a delaminated form and gradually decreases with the increasing depth from the contact surface. Such gradient strain energy could give rise to lattice rotation in the tribo-deformed structure. Figure 8(a) measures the evolution of misorientation angle from the bottom grain boundary of the α_P structure to the

wear surface, and the accumulated lattice rotation could reach 17.9° at S6 relative to the bottom S1.

The associated dislocation structure was analyzed by tilting the specimen to the two-beam condition of $g = 01\bar{1}1$, and a prismatic slip band across the α_P grain with ~240 nm in width is revealed by the bright-field TEM image (Fig. 8(b)). Scattered dislocation lines are generated in the region between the slip band and the adjacent grain boundary on the right.

From S1 to S3 (Fig. 8(b)), the prismatic slip deformation is activated in response to the tribological shear stress, and the associated domain exhibits a stable misorientation angle. Thereafter, the dislocation lines tangling and evolving into the tangled dislocation cluster associates with a significant rising in lattice rotation from S3 to S4. While in the TDL, the lattice is severely strained by the density of tangled dislocations, which promotes further grain rotation from S4 to S6 significantly. The lattice orientation at each site is represented by a hexagonal lattice (Fig. 8(b)), of which the *c*-axis is highlighted with an arrow. Of note is that the *c*-axis direction of each site along the indicated path is aligned in almost the same direction, which suggests that the α_P structure could rotate with the *c*-axis as the rotation axis in response to the surface reciprocating shear deformation.

The outmost layer (~200 nm) in slip zone consisting of nanograins was unraveled by the t-EBSD technic beneath the oxidization layer (Figs. 9(a) and 9(b)), and the microstructures were gradually coarsened as the distance to the wear surface increased. Beneath the nanostructured layer, it exhibits a deformed grain with ~5° lattice rotation in comparison to those of the bottom original locations (P_{11}, P_{21}, and P_{31}) adjacent to the grain boundary (Fig. 9(c)). It is noteworthy that the lattice structure exhibits a sustained growth of misorientation along path 2 without forming a conspicuous plateau domain resembling the misorientation evolution along paths 1 and 3. In general, the grain rotates in the same manner as the aforementioned grain rotation beneath the stick zone: with the *c*-axis of hexagonal close-packed structure as the rotation axis.
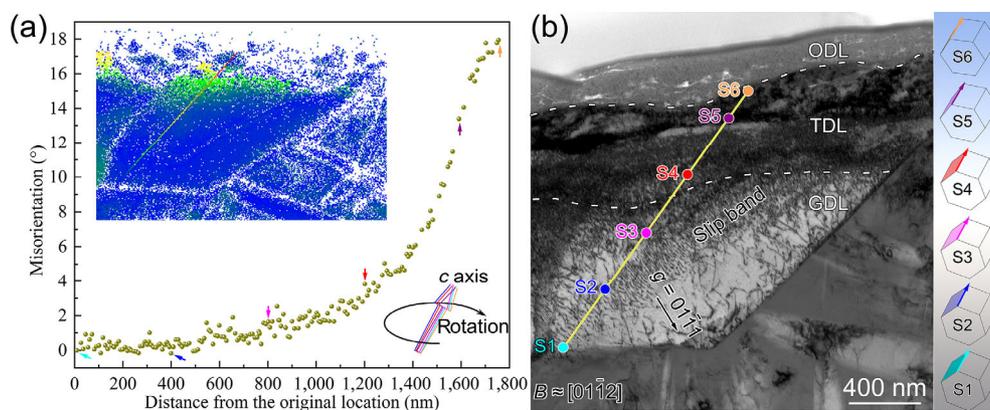

Fig. 8 (a) Misorientation evolution relative to indicated origins and (b) bright-field TEM image of evolved dislocation morphology within deformed α grain. Note: *B* is the beam direction.
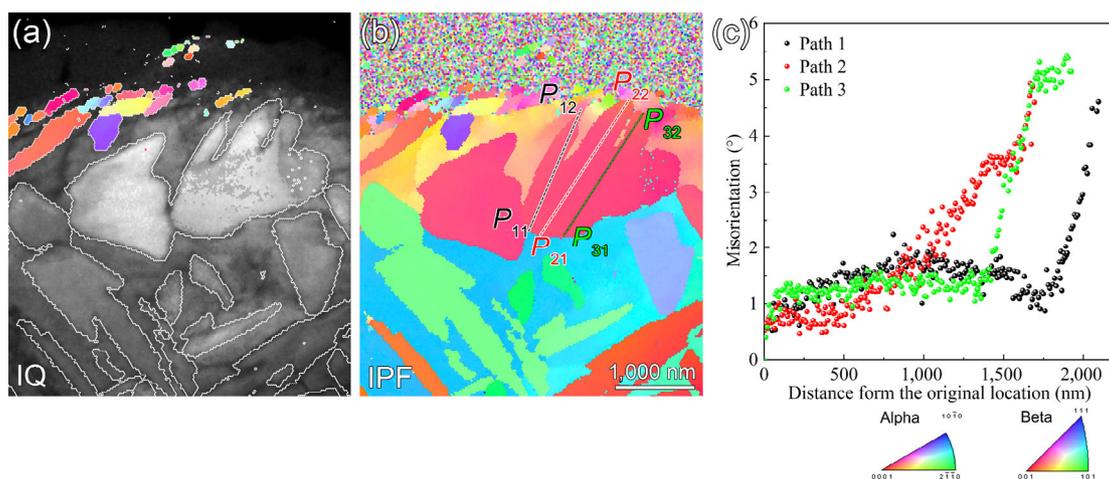

Fig. 9 (a) Image quality (IQ) mapping with highlighted surface nano α grains, (b) IPF showing the grain orientation, and (c) misorientation evolution relative to indicated origins (P_{i1}, *i* = 1, 2, and 3) within deformed α grain.

The bright-field TEM photograph (Fig. 10(a)) demonstrates the morphology of nanograins within the topmost wear ridge, and nanograins are separated by dislocation arrays indicated by the arrows. While in the deformed grain, deformed microstructures revealed by the dark image (Fig. 10(b)) are obtained under two-beam condition and can be categorized into dislocation lines and tangled dislocations based on their morphologies. Interestingly, the underlying mechanisms governing the lattice rotation along the specified paths (Fig. 9) are different [49]. Similar to the strain response against the tribological shear stress within the stick zone (Fig. 8), the slip deformation can hardly give rise to the lattice rotation (plateau in paths 1 and 3), which is mainly caused by the tangled dislocation.

Deformed microstructures from coarse to nanograins layer had been furtherly analyzed to study the nano-crystallization process under fretting wear loading. Figure 11 shows the t-EBSD results of the grains in the vicinity beneath the top surface-oxidized layer. In the IPF mapping, the grains are numbered from Grain 1 to Grain 14. The tribo-strain within deformed grains was evaluated by the 1st KAM method. As indicated by the arrow in Grain 1, intermittent grain boundary segments associated with the high KAM band are generated, of note is that the generated grain boundary exhibits a gradient misorientation, wherein the 2°–5° LAGB section demonstrates a discontinuity shape and is separated by short segments with a misorientation higher than

5° (high angle grain boundary (HAGB)). The HAGB section below is well established and presents in a continuous shape. Similarly, clusters of LAGB segments are generated in the vicinity beneath Grains 6, 7, and 8 as well. As such, the early fretting damage in titanium alloy could result in the formation of LAGB in the prior deformed grains [16].

The grain refinement in the TDL was regarded as a strain-induced dynamic recrystallization process [50, 51], which could be evaluated by the GOS value of related grains. The GOS values of α and β structures in the TDL are compared in Fig. 11 by coloring each grain by its GOS values, and the value of 5° herein is taken as the threshold value to separate the dynamically recrystallized grains (GOS < 5°) from deformed ones (GOS > 5°) [52]. Accordingly, nano α and β grains in the TDL are well established. Besides, the grains just beneath the topmost nanostructured layer exhibit relatively higher GOS values and accumulated strain energy as well, especially for the grains containing LAGB segments, such as α grains numbered 6, 12, 13 and β grains numbered 8, 9, and 11.

In the TDL, the dislocation morphologies of the above relevant grains were analyzed using the TEM, as shown in Fig. 12. Grains were numbered referring to Fig. 11, and the marker "R" above Grain 5 was used as the same location reference as in Fig. 11. Most of the grains in this domain are highly deformed and exhibit a high density of dislocations inside. Grain 11 (Fig. 12(a)) is undergoing the grain refinement process caused by the formation of banded high-density
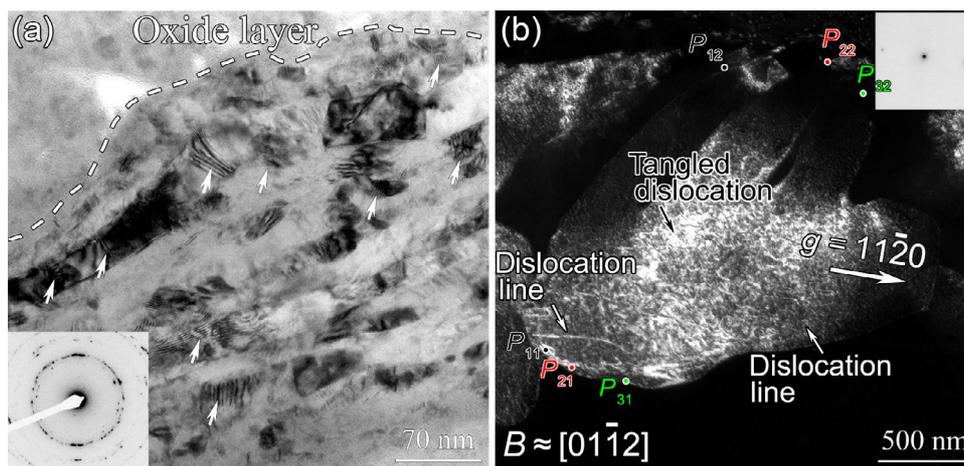

Fig. 10 (a) Bright-field TEM image of topmost nanostructured layer and (b) weak beam dark-field TEM image showing the dislocation morphologies within selected α grain.
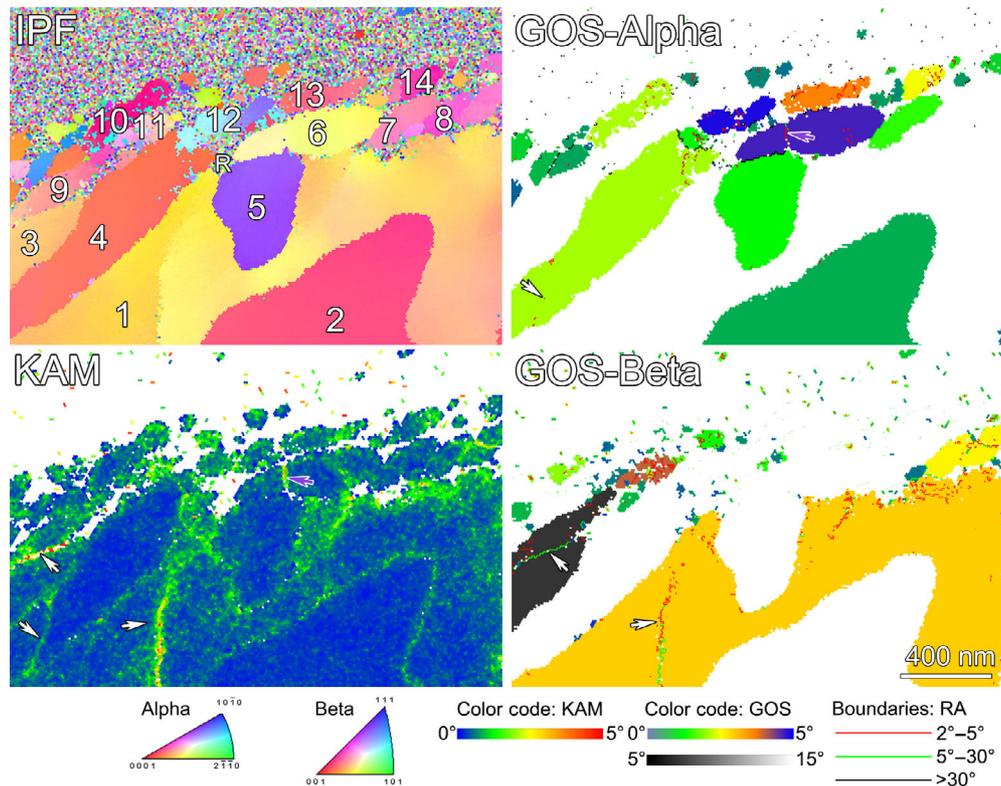
Fig. 11 t-EBSD characterization results demonstrating the grain orientation, KAM, and grain orientation spread (GOS) from the topmost nanostructured layer to the underlying deformed layer. Note: RA is the rotation angle.

dislocation arrays highlighted with the dashed lines. Correspondingly, the GOS value of grain has been measured to be ~4.04° by the t-EBSD technic (Fig. 11), and clusters of LAGB segment interior can be recognized. Similarly, LAGB segments have been identified clearly in Grain 1. In the vicinity of LAGBs, as revealed by the magnified dark-field photograph (Fig. 12(b)), the lattice exhibits high accumulated strain energy, and the associated dislocation structures are aligned to form parallel arrays.

The formation of grain boundaries regarding the evolution of dislocation morphology under severe plastic deformation has been addressed by Li et al. [53]. Initial strain response of the metallic structure is mainly in the form of slip deformation, such as the dislocation line structures (Fig. 10(b)). The accumulation of plastic strain could give rise to the dislocation densities, and promote the interaction of early slip dislocations to form tangled dislocation structures, thereby altering the associated local lattice orientation. However, due to the relative homogeneous strain distribution within the tangled dislocation domain,

grain boundary structures can hardly take shape. Thereafter, dislocation structures are furtherly aligned to minimize the dislocation energy by forming the dislocation arrays, as presented in Fig. 12(b), generating a short-range high strain gradient, which necessitates the formation of LAGB segments to separate the misoriented domains on both sides. The formation of indicated LAGB that outlined the high deformed volume within the prior host Grain 1 (Fig. 12(c)) and the grain boundary within Grain 6 (Fig. 12(d)) has been unraveled in much the same manner. However, as demonstrated in Fig. 11, the indicated grain boundary within Grain 6 evolves from the lower angle misoriented range on the bottom side into the higher angle misoriented range in the upper range. The GOS value is ~4.65°, which is close to the critical value (GOS < 5°) in evaluating the dynamic recrystallization process of Mg alloy [52], but higher than the value (GOS < 1.3°) that used to identify the dynamically recrystallized grains in titanium [54]. The above t-EBSD and TEM characterization results might suggest that the gradient misoriented grain
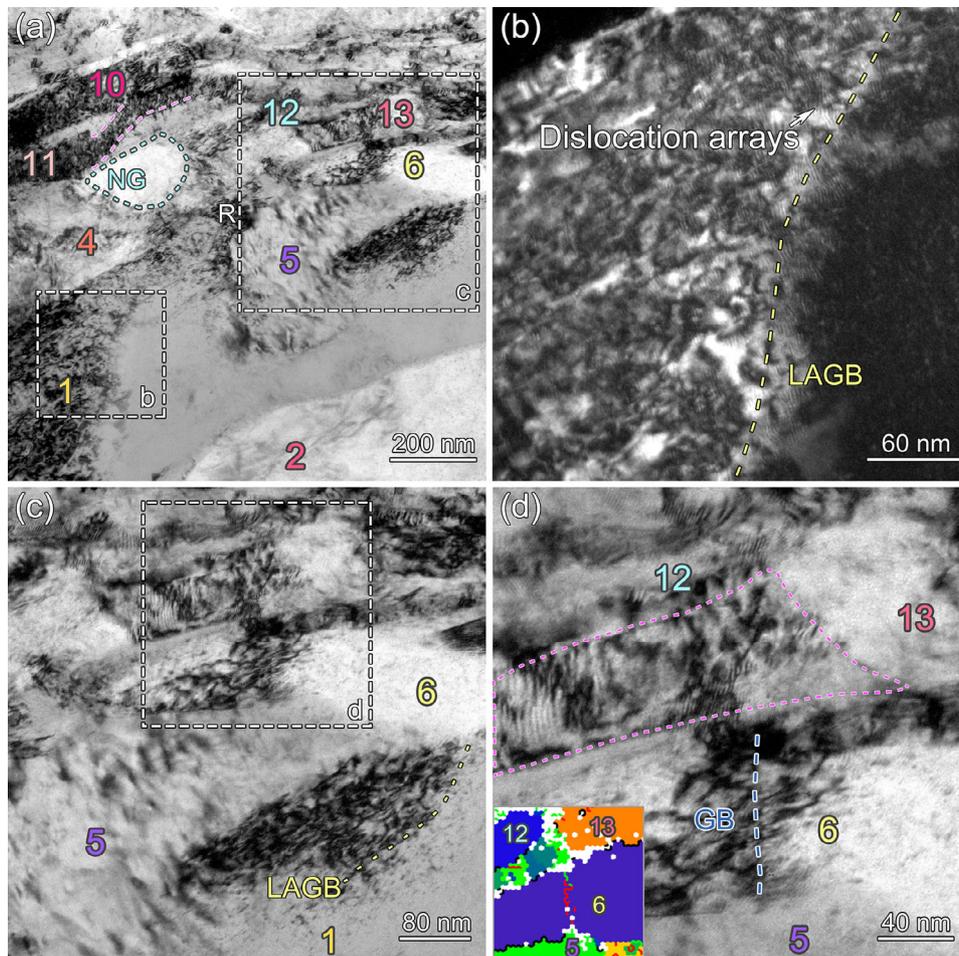
Fig. 12 (a) Bright-field TEM image from the topmost nanostructured layer to the beneath deformed coarse grain, (b) dark-field TEM image and (c) bright-field TEM image showing the dislocation arrays adjacent to the LAGBs that are enclosed with the rectangles in (a), and (d) magnified view of gradient grain boundary within Grain 6 and adjacent deformed structures. Note: NG is nanograin, and GB is grain boundary.

boundary (from LAGB to HAGB domains) is generated as a boundary to minimize the accumulated strain energy and separate the severely deformed slip deformed domains within the prior grain experiencing a dynamic crystallization process. Driven by the tribological shear stress, the gradient grain boundary could *in-situ* transform into a full high angle misoriented grain boundary thereafter to subdivide the grain into finer structures. As a result, dynamically recrystallized nanograins are generally enclosed by HAGBs consisting of high-density dislocations [55, 56], like the highlighted equiaxed nanograin (Fig. 12(a)), of which the inner grain exhibits a low strain energy.

Thus, based on the above-mentioned results and analysis, the microstructural evolution process of bimodal titanium alloy subjected to the fretting wear

fatigue loading regarding the dislocation morphology can be schematically illustrated in Fig. 13. Initially, the grain undergoes slip deformation, and the dislocation lines are generated within the grain. The accumulated tribo-strain tangles the dislocation lines, giving rise to lattice rotation to accommodate the associate strain continuity. Thereafter, dislocation structures will be aligned to generate a misoriented substructure containing parallel dislocation arrays within the highly deformed prior host grain, favoring the formation of sub-boundary segments with a low angle misorientation to the adjacent matrix. Furtherly, the LAGB segments will be connected in response to the more severe localized strain gradient and *in-situ* evolve into HAGB to separate the severely deformed domain from the vicinity and refine the prior host grain.
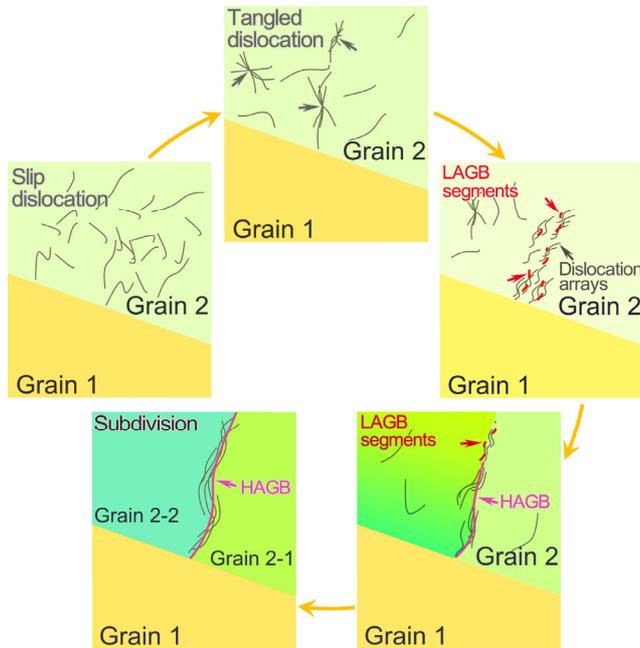
Fig. 13 Schematic illustration indicating the grain refinement process and the associated evolution in dislocation morphology in Grain 2.

4 Conclusions

By employing the t-EBSD and TEM, the microstructural evolution and oxidation behavior of α/β titanium alloy subjected to torsional fretting fatigue loading were studied. The main conclusions can be drawn as follows:

1) The initial contact region could fade away over 10^8 cycles of fretting wear under the given test condition. Besides, the maximum depth of the fretting damaged area is close to the interface of contact/slip and can reach ~15.8 μm.

2) Cracking interfaces of the oxidation domain and topmost nanograins facilitate surface degradation, thereby promoting the stress mismatch along the contact area boundary and giving rise to the formation of macro cracks with the assistance of oxygen pick-up at the crack tip thereafter.

3) Grain rotation can be recognized in the subregion within the deformed grain where tangled dislocations are formed, and further deformation could result in the formation of nanoscale misoriented lattice associated with parallel dislocation arrays, producing the LAGB segments in the related regions.

4) The α_P structure could rotate with the *c*-axis as the rotation axis in response to the surface reciprocating the tribological shear stress.

5) Nanograins in the TDL are separated by non-equilibrium HAGB formed by high-density dislocation arrays that *in-situ* evolved from prior LAGB, while the stored strain energy interior is comparatively low.

References

[1] Boyer R R. An overview on the use of titanium in the aerospace industry. *Mater Sci Eng A* **213**(1–2): 103–114 (1996)

[2] Pao P, Imam M A, Jones H, Bayles R, Feng J. Effect of oxygen on stress-corrosion cracking and fatigue crack growth of Ti-6211. In: Proceedings of the 11th World Conference on Titanium (Ti-2007 Science and Technology), Kyoto, Japan, 2007: 279–282.

[3] Hoeppner D W, Goss G L. A fretting-fatigue damage threshold concept. *Wear* **27**(1): 61–70 (1974)

[4] Budinski K G. Tribological properties of titanium alloys. *Wear* **151**(2): 203–217 (1991)

[5] Antoniou R A, Radtke T C. Mechanisms of fretting-fatigue of titanium alloys. *Mater Sci Eng A* **237**(2): 229–240 (1997)

[6] Swalla D R, Neu R W, McDowell D L. Microstructural characterization of Ti–6Al–4V subjected to fretting. *J Tribol* **126**(4): 809–816 (2004)

[7] Abedini M, Ghasemi H M, Nili Ahmadabadi M, Mahmudi R. Effect of phase transformation on the wear behavior of NiTi alloy. *J Eng Mater Technol* **132**(3): 031010 (2010)

[8] Luo J S, Sun W T, Duan R X, Yang W Q, Chan K C, Ren F Z, Yang X S. Laser surface treatment-introduced gradient nanostructured TiZrHfTaNb refractory high-entropy alloy with significantly enhanced wear resistance. *J Mater Sci Technol* **110**: 43–56 (2022)

[9] Liu Z L, Patzig C, Selle S, Höche T, Gumbsch P, Greiner C. Stages in the tribologically-induced oxidation of high-purity copper. *Scripta Mater* **153**: 114–117 (2018)

[10] Lehmann J S, Schwaiger R, Rinke M, Greiner C. How tribo-oxidation alters the tribological properties of copper and its oxides. *Adv Mater Interfaces* **8**(1): 2001673 (2021)

[11] Eder S J, Rodríguez Ripoll M, Cihak-Bayr U, Dini D, Gachot C. Unraveling and mapping the mechanisms for near-surface microstructure evolution in CuNi alloys under sliding. *ACS Appl Mater Interfaces* **12**(28): 32197–32208 (2020)

[12] Haug C, Ruebeling F, Kashiwar A, Gumbsch P, Kübel C, Greiner C. Early deformation mechanisms in the shear affected region underneath a copper sliding contact. *Nat Commun* **11**(1): 839 (2020)

[13] Das S, Riahi A R, Meng-Burany X, Morales A T, Alpas A T. High temperature deformation and fracture of tribo-layers on the surface of AA5083 sheet aluminum–magnesium alloy. *Mater Sci Eng A* **531**: 76–83 (2012)

[14] ang Y, Lei T Q, Liu J J. Tribo-metallographic behavior of high carbon steels in dry sliding III. Dynamic microstructural changes and wear. *Wear* **231**(1): 20–37 (1999)

[15] Chen K M, Zhou Y, Li X X, Zhang Q Y, Wang L, Wang S Q. Investigation on wear characteristics of a titanium alloy/steel tribo-pair. *Mater Design 2015* **65**: 65–73 (2015)

[16] Swalla D R, Neu R W. Fretting damage assessment of titanium alloys using orientation imaging microscopy. *Tribol Int* **39**(10): 1016–1027 (2006)

[17] Glaeser W A. Wear experiments in the scanning electron microscope. *Wear* **73**(2): 371–386 (1981)

[18] Bill R C, Wisander D. Recrystallization as a controlling process in the wear of some F.C.C. metals. *Wear* **41**(2): 351–363 (1977)

[19] Prasad S V, Michael J R, Battaile C C, Majumdar B S, Kotula P G. Tribology of single crystal nickel: Interplay of crystallography, microstructural evolution, and friction. *Wear* **458–459**: 203320 (2020)

[20] Yang L, Cheng Z, Zhu W W, Zhao C C, Ren F Z. Significant reduction in friction and wear of a high-entropy alloy via the formation of self-organized nanolayered structure. *J Mater Sci Technol* **73**: 1–8 (2021)

[21] Xin L, Wang Z H, Li J, Lu Y H, Shoji T. Microstructural characterization of subsurface caused by fretting wear of Inconel 690TT alloy. *Mater Charact* **115**: 32–38 (2016)

[22] Xin L, Liang X, Han Y M, Lu Y H, Shoji T. Investigation into the fretting corrosion of alloy 690 TT against type 304 stainless steel in high temperature pure water under partial slip conditions. *Tribol Int* **134**: 93–101 (2019)

[23] Mao B, Zhang X, Menezes P L, Liao Y L. Anisotropic microstructure evolution of an AZ31B magnesium alloy subjected to dry sliding and its effects on friction and wear performance. *Materialia* **8**: 100444 (2019)

[24] Ming H L, Liu X C, Yan H L, Zhang Z M, Wang J Q, Gao L X, Lai J, Han E H. Understanding the microstructure evolution of Ni-based superalloy within two different fretting wear regimes in high temperature high pressure water. *Scripta Mater* **170**: 111–115 (2019)

[25] Rau J S, Balachandran S, Schneider R, Gumbsch P, Gault B, Greiner C. High diffusivity pathways govern massively enhanced oxidation during tribological sliding. *Acta Mater* **221**: 117353 (2021)

[26] Han Q N, Rui S S, Qiu W H, Ma X F, Su Y, Cui H T, Zhang H J, Shi H J. Crystal orientation effect on fretting fatigue induced geometrically necessary dislocation distribution in Ni-based single-crystal superalloys. *Acta Mater* **179**: 129–141 (2019)

[27] Li Z Y, Liu X L, Wu G Q, Sha W. Observation of fretting fatigue cracks of Ti$_6$Al$_4$V titanium alloy. *Mater Sci Eng A* **707**: 51–57 (2017)

[28] Chakravarty S, Andrews R G, Painaik P C, Koul A K. The effect of surface modification on fretting fatigue in Ti Alloy turbine components. *JOM* **47**(4): 31–35 (1995)

[29] Teng Z J, Liu H Q, Wang Q Y, Huang Z Y, Starke P. Fretting behaviors of a steel up to very high cycle fatigue. *Wear* **438–439**: 203078 (2019)

[30] Teng Z J, Wu H R, Huang Z Y, Starke P. Effect of mean stress in very high cycle fretting fatigue of a bearing steel. *Int J Fatigue* **149**: 106262 (2021)

[31] Wagner D, Cavalieri F J, Bathias C, Ranc N. Ultrasonic fatigue tests at high temperature on an austenitic steel. *Propuls Power Res* **1**(1): 29–35 (2012)

[32] Tan X P, Kok Y, Toh W Q, Tan Y J, Descoins M, Mangelinck D, Tor S B, Leong K F, Chua C K. Revealing martensitic transformation and α/β interface evolution in electron beam melting three-dimensional-printed Ti–6Al–4V. *Sci Rep* **6**: 26039 (2016)

[33] Liu H Q, Wang H M, Huang Z Y, Wang Q Y, Chen Q. Comparative study of very high cycle tensile and torsional fatigue in TC17 titanium alloy. *Int J Fatigue* **139**: 105720 (2020)

[34] Mayer H. Recent developments in ultrasonic fatigue. *Fatigue Fract Eng M* **39**(1): 3–29 (2016)

[35] Cai Z B, Zhu M H, Shen H M, Zhou Z R, Jin X S. Torsional fretting wear behaviour of 7075 aluminium alloy in various relative humidity environments. *Wear* **267**(1–4): 330–339 (2009)

[36] Singh K, Mahato A, Tiwari M. Transition from mixed stick–slip to gross–slip regime in fretting. *Tribol Int* **165**: 107338 (2022)

[37] Yuan X L, Li G, Zhang X Y, Pu J, Ren P D. An experimental investigation on fretting wear behavior of copper–magnesium alloy. *Wear* **462–463**: 203497 (2020)

[38] Shen M X, Xie X Y, Cai Z B, Zheng J F, Zhu M H. An experiment investigation on dual rotary fretting of medium carbon steel. *Wear* **271**(9–10): 1504–1514 (2011)

[39] Cai Z B, Zhu M H, Zhou Z R. An experimental study torsional fretting behaviors of LZ50 steel. *Tribol Int* **43**(1–2): 361–369 (2010)

[40] Zeng D F, Zhang Y B, Lu L T, Zou L, Zhu S Y. Fretting wear and fatigue in press-fitted railway axle: A simulation study of the influence of stress relief groove. *Int J Fatigue* **118**: 225–236 (2019)

[41] Majzoobi G H, Abbasi F. On the effect of contact geometry on fretting fatigue life under cyclic contact loading. *Tribol Lett* **65**(4): 125 (2017)

[42] Fouvry S, Kapsa P, Vincent L. Quantification of fretting damage. *Wear* **200**(1–2): 186–205 (1996)

[43] Philip J T, Kumar D, Mathew J, Kuriachen B. Tribological investigations of wear resistant layers developed through EDA and WEDA techniques on Ti$_6$Al$_4$V surfaces: Part II—High temperature. *Wear* **466–467**: 203540 (2021)

[44] Baydoun S, Fouvry S. An experimental investigation of adhesive wear extension in fretting interface: Application of the contact oxygenation concept. *Tribol Int* **147**: 106266 (2020)

[45] Besenbacher F, Nørskov J K. Oxygen chemisorption on metal surfaces: General trends for Cu, Ni and Ag. *Prog Surf Sci* **44**(1): 5–66 (1993)

[46] Satko D P, Shaffer J B, Tiley J S, Semiatin S L, Pilchak A L, Kalidindi S R, Kosaka Y, Glavicic M G, Salem A A. Effect of microstructure on oxygen rich layer evolution and its impact on fatigue life during high-temperature application of α/β titanium. *Acta Mater* **107**: 377–389 (2016)

[47] Parthasarathy T A, Porter W J, Boone S, John R, Martin P. Life prediction under tension of titanium alloys that develop an oxygenated brittle case during use. *Scripta Mater* **65**(5): 420–423 (2011)

[48] Pilchak A L, Porter W J, John R. Room temperature fracture processes of a near-α titanium alloy following elevated temperature exposure. *J Mater Sci* **47**(20): 7235–7253 (2012)

[49] Huang X, Hansen N. Grain orientation dependence of microstructure in aluminium deformed in tension. *Scripta Mater* **37**(1): 1–7 (1997)

[50] Yao B, Han Z. Effect of counterface materials on dynamic recrystallized structure and wear resistance of nanostructured Cu. *Tribol Int* **113**: 426–432 (2017)

[51] Dryzek J, Wróbel M. Detection of tribolayer in pure iron using positron annihilation and EBSD techniques. *Tribol Int* **144**: 106133 (2020)

[52] Hadadzadeh A, Mokdad F, Wells M A, Chen D L. A new grain orientation spread approach to analyze the dynamic recrystallization behavior of a cast-homogenized Mg–Zn–Zr alloy using electron backscattered diffraction. *Mater Sci Eng A* **709**: 285–289 (2018)

[53] Li H X, Ii S, Tsuji N, Ohmura T. Direct observation of grain boundary formation in bcc iron through TEM *in situ* compression test. *Scripta Mater* **207**: 114275 (2022)

[54] Yan C K, Feng A H, Qu S J, Cao G J, Sun J L, Shen J, Chen D L. Dynamic recrystallization of titanium: Effect of pre-activated twinning at cryogenic temperature. *Acta Mater* **154**: 311–324 (2018)

[55] Sakai T K, Belyakov A, Kaibyshev R, Miura H, Jonas J J. Dynamic and post-dynamic recrystallization under hot, cold and severe plastic deformation conditions. *Prog Mater Sci* **60**: 130–207 (2014)

[56] Zhao Z Y, Guan R G, Shen Y F, Bai P K. Grain refinement mechanism of Mg–3Sn–1Mn–1La alloy during accumulative hot rolling. *J Mater Sci Technol* **91**: 251–261 (2021)

Hanqing Liu. He received his BS in theoretical and applied mechanics from Lanzhou University, China, in 2013, ME in solid mechanics in 2016 and Ph.D. in aerospace mechanics and engineering in 2019 from Sichuan University, China. He worked as a JSPS Postdoctoral Fellow at Kyushu University, Japan, until November 2022. He joined the University of Oxford, UK, in January 2023 as a Postdoctoral Research Fellow. His research interests include mechanical behavior and microstructural characterization of materials that experienced harsh environments.

Qingyuan Wang. He received his Ph.D. from Ecole Centrale Paris, France, in 1998. He worked at Sichuan University, China, as a professor since 2003. His research interests include very high cycle fatigue; mechanical behavior of materials and structures; experimental mechanics of solid.

Lang Li. He received his Ph.D. from Sichuan University, China, in 2018, working as an associate researcher in the department of mechanics of Sichuan University now. His research interests include experimental mechanics of solid, and microstructural behavior of in-service materials.